

Dual Protection Layer Strategy to Increase Photoelectrode–Catalyst Interfacial Stability: A Case Study on Black Silicon Photoelectrodes

Fan Yang, Jeffery A. Aguiar, Michael Fairchild, Waltteri Vakki, Sabrina Younan, Yinghua Zhou, Linhai Zhuo, and Jing Gu*

Photoelectrode degradation under harsh solution conditions continues to be a major hurdle for long-term operation and large-scale implementation of solar fuel conversion. In this study, a dual-layer TiO_2 protection strategy is presented to improve the interfacial durability between nanoporous black silicon and photocatalysts. Nanoporous silicon photocathodes decorated with catalysts are passivated twice, providing an intermediate TiO_2 layer between the substrate and catalyst and an additional TiO_2 layer on top of the catalysts. Atomic layer deposition of TiO_2 ensures uniform coverage of both the nanoporous silicon substrate and the catalysts. After 24 h of electrolysis at $\text{pH} = 0.3$, unprotected photocathodes layered with platinum and molybdenum sulfide retain only 30% and 20% of their photocurrent, respectively. At the same pH , photocathodes layered with TiO_2 experience an increase in photocurrent retention: 85% for platinum-coated photocathodes and 91% for molybdenum sulfide-coated photocathodes. Under alkaline conditions, unprotected photocathodes experience a 95% loss in photocurrent within the first 4 h of electrolysis. In contrast, TiO_2 -protected photocathodes maintain 70% of their photocurrent during 12 h of electrolysis. This approach is quite general and may be employed as a protection strategy for a variety of photoabsorber–catalyst interfaces under both acidic and basic electrolyte conditions.

sunlight is sufficient to supply the ≈ 18 TW of energy required to meet our current global energy needs^[2] and sustain our society's projected energy demands (≈ 80 TW to carry society through the end of this century).^[1–4] This enormous potential within solar energy systems has aroused great interest in the scientific community. Numerous strategies to harvest solar energy have been proposed and studied, such as photovoltaics,^[5] water splitting,^[6–9] and artificial photosynthesis of organic molecules.^[10] Of particular interest to this group is photoelectrochemical (PEC) hydrogen production, by means of photo-induced electrochemical conversion. PEC systems prove to be promising and practical due to hydrogen's abilities as a clean chemical fuel that can be stored, transferred, and redistributed to meet our ever increasing energy demands.

A key component of PEC systems is the presence of an efficient photoabsorber able to instantly and effectively absorb and convert solar irradiation into electrical energy. Silicon (Si) has been widely investigated and employed in PEC systems due


to its high abundance and low cost.^[11,12] Its narrow bandgap of 1.12 eV suggests that Si is suitable to absorb a wide wavelength range, making it advantageous in comparison with other semiconductor materials. Si's bandgap is slightly lower than overall water splitting energetics (1.23 eV), while its conduction

1. Introduction

Solar energy is one of the most abundant, clean, and sustainable energy resources on Earth. Roughly 100 000 TW of solar energy strikes our planet annually.^[1] Only $\approx 0.1\%$ of that incident

Dr. F. Yang, M. Fairchild, W. Vakki, S. Younan,
Prof. Y. Zhou, Prof. L. Zhuo, Prof. J. Gu
Department of Chemistry and Biochemistry
San Diego State University
5500 Campanile Drive, San Diego, CA 92182-1030, USA
E-mail: jgu@sdsu.edu

Dr. J. A. Aguiar
Idaho National Laboratory
Nuclear Materials Department
2525 Fremont Avenue, Idaho Falls, ID 83415, USA

 The ORCID identification number(s) for the author(s) of this article can be found under <https://doi.org/10.1002/admi.201802085>.

Prof. Y. Zhou
The Key Laboratory of Functional Molecular Solids
Ministry of Education
Anhui Laboratory of Molecule-Based Materials (State Key
Laboratory Cultivation Base)
College of Chemistry and Materials Science
Anhui Normal University
Wuhu 241000, China

Prof. L. Zhuo
Department of Chemistry and Chemical Engineering
Taishan University
Taian 271021, China

DOI: 10.1002/admi.201802085

band is energetically more negative than the proton reduction potential.^[13] This makes Si an ideal candidate for the hydrogen evolution reaction (HER). High reflectance experienced by planar Si limits potential large-scale production and integration of efficient Si-based PEC systems. Compared with planar Si, nanoporous black Si exhibits many attractive properties, such as low reflectance and high surface area.^[14,15] Recently, nanoporous black Si has shown excellent PEC activity resulting from robust light absorption efficiency and charge transport properties.^[16–19] Unfortunately, Si-based photoelectrodes often suffer from poor stability due to spontaneous silicon oxide (SiO₂) formation upon exposure to air.^[3] While black Si contains a greater chemically active surface area, this increased surface area also speeds up its degradation process, making it more challenging to protect. Previous efforts to decrease the rate of degradation by addition of protection layers, such as TiO₂ or Al₂O₃, have been attempted.^[19–26] However, these efforts lack evidence of stability under electrolysis for more than 12 h and nanoporous black Si-based photocathodes continue to suffer from degradation under prolonged electrolysis (Table S1, Supporting Information).

Another vital constituent to PEC systems is the presence of a robust catalyst. Successful catalysts must be able to lower the energy barrier in the chemical reaction of interest, such as HER and oxygen evolution reactions (OER). Previous conventional protection schemes via atomic layer deposition (ALD) apply only one atomic protection layer between the substrate and catalyst. This method focuses on protecting the substrate, but ignores the necessity to protect the photoelectrode–catalyst interface. A common problem for such interfaces is their tendency toward catalyst decomposition, aggregation, and/or detachment from supporting substrates.^[27] Platinum (Pt) is a well-known catalyst that is commonly used for HER, yet Pt's possible aggregation and detachment from the photoelectrode–Pt interface is rarely discussed. Amorphous molybdenum disulfide (MoS_x) is another widely employed catalyst in many applications whose instability is also well recognized. To date, methods to improve either catalyst's stability have yet to be well studied.^[28–30] Stabilizing the catalyst and the photoabsorber–catalyst interface is equally as important as stabilizing photoabsorber systems. Furthermore, maintaining the structural integrity of those materials and interfaces is a critical issue that needs to be resolved before any commercialization of PEC systems may be achieved.^[4,31,32]

In this work, a dual TiO₂ layer strategy is proposed to protect photoelectrode–catalyst interfaces. The catalysts are sandwiched between the two layers of TiO₂, ensuring optimal protection of the photoabsorber–catalyst interface. Significant durability enhancement is achieved in both strong acid and strong base conditions for both catalysts studied herein. The proposed dual-protection method is expected to be further integrated into a general strategy for stabilization of other heterogeneous or homogeneous catalytic interfaces implemented in a vast array of energy conversion applications.

2. Results and Discussion

The instability of the bSi/Pt photoelectrode over long-term electrolysis is a well-known dilemma.^[16–18] To understand the reasoning behind degradation, scanning electron microscopy

(SEM) was used to visualize the surface morphologies of the bSi/Pt electrode before and after PEC electrolysis. **Figure 1A** shows nanoporous black silicon (bSi) as the photoabsorber substrate. Nanoporous bSi was prepared using the metal-assisted chemical etching (MACE) method^[17,33–36] (experimental details are provided in Supporting Information). Nanopores with an average diameter of 30–80 nm and depth of 700–800 nm were densely distributed perpendicularly to the (100) Si surface (**Figure 1A**; **Figure S1**, Supporting Information). The nanoporous structure increases Si's surface area and decreases Si's light reflectivity by trapping incident light. Deposited Pt nanoparticles (NPs) show uniform distribution across the substrate's surface, covering the majority of the nanoporous structure before electrolysis (**Figure 1B**). After 24 h electrolysis, the Pt NPs aggregate into granular-textured clusters and partial re-exposure of the nanopores occurred. This indicates a rearrangement of the heterogeneous Pt catalyst during HER (**Figure 1C**). After 76 h electrolysis, Pt NP aggregation continued and SiO₂ accumulated on the surface (**Figure 1D**; **Figure S2**, Supporting Information). Though the cause of Pt rearrangement is unclear, sintering and leaching of NPs are common problems in catalysis due to either particle migration or Ostwald ripening.^[37] Thus, agglomeration and spalling of Pt NPs at the Si/Pt interface is a potential contributing factor to the photocathode's photocurrent loss (**Figure 2A**) and decomposition at the semiconductor/catalyst interface after long-term electrolysis.

To increase the bSi/Pt photocathode's stability, a 20 nm TiO₂ thin film intermediate layer was deposited on the bSi substrate at 100, 200, and 300 °C via ALD (fabricated electrodes are denoted as bSi/TiO₂-X/Pt, X = ALD temperature), similar to previous literature.^[19–21,24–26,32] The surface morphology of bSi/TiO₂/Pt electrodes is further investigated in **Figure S3** in the Supporting Information. After electrolysis, the morphology and size of Pt NPs on all intermediate-layer-protected photocathodes did not change dramatically (**Figure S3**, Supporting Information). Instead, the diameter of Pt NPs on bSi/TiO₂/Pt produced at 100, 200, and 300 °C shift from 20.5, 21.1, and 22.6 nm to 20.9, 17.2, and 22.2 nm, respectively (**Figure S4**, Supporting Information). In accordance with the SEM images, a decrease in particle density is witnessed in all three electrodes after 24 h of electrolysis (**Figure S3**, Supporting Information). This decrease may further affect the photoelectrode's performances. The bSi/TiO₂-300D/Pt electrode, where D represents °C, exhibits the smallest loss of Pt NPs and the most photocurrent retention during 24 h electrolysis (**Figure S5**, Supporting Information). The corresponding photocurrent retentions of bSi/TiO₂-100D/Pt, bSi/TiO₂-200D/Pt, and bSi/TiO₂-300D/Pt are 40%, 55%, and 60%, respectively. We conclude that the conventional intermediate layer does not prevent catalyst leaching. Therefore, an additional protection layer on top of the catalyst layer is necessary to maintain the integrity of a photoelectrode–catalyst interface.

It is possible for the conventional one-layer TiO₂ protection scheme to suffer from instability prior to electrolysis, especially on bSi surfaces. In previous research,^[16,17,19] Si-based photoelectrodes constructed with and without a protection layer often required etching in dilute hydrofluoric (HF) solution (often 5 wt%), prior to catalyst deposition and PEC measurements, to

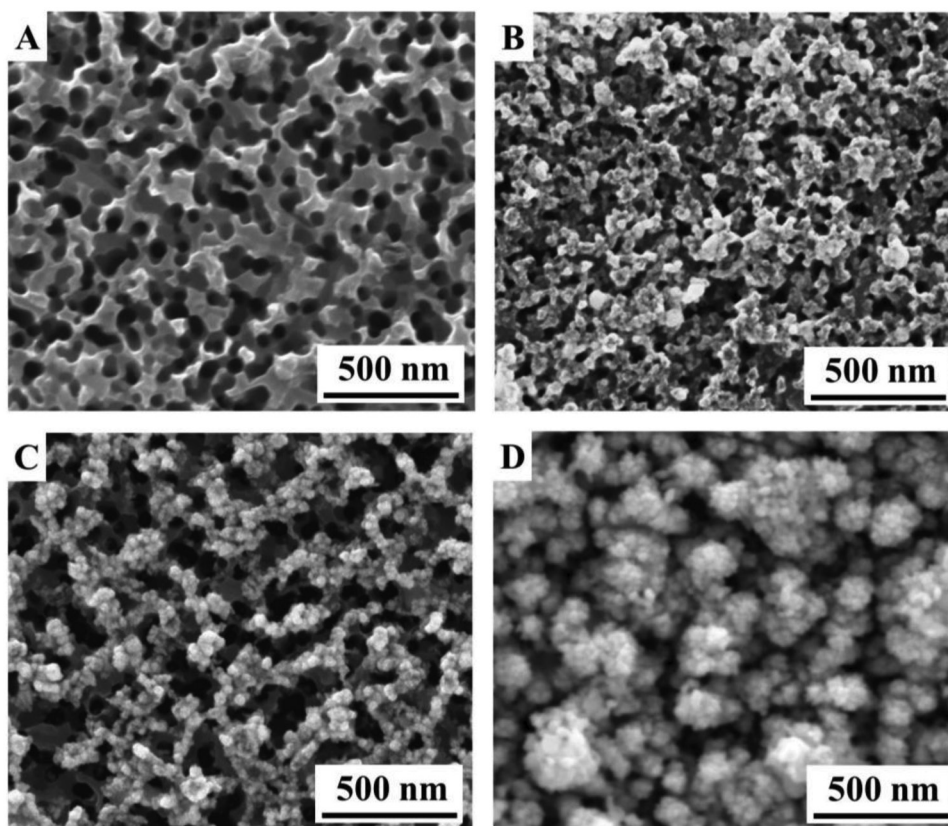


Figure 1. SEM planar view of A) bSi, B) bSi with Pt catalyst (bSi/Pt), C) bSi/Pt photocathode after 24 h electrolysis, and D) bSi/Pt photocathode after 76 h electrolysis.

remove SiO_2 and other surface contaminants. Etching can be problematic for protective layers, however, due to the possibility of TiO_2 to react with the etchant solution,^[38] which would result with partial loss of TiO_2 . Increase in deposition temperature from 100 to 300 °C increases the crystallinity of TiO_2 ,^[39,40] which helps reduce TiO_2 's decomposition rate (Figures S6 and S7, Supporting Information). After etching in 5 wt% HF for 90 s, 25%, 50%, and 75% of the Ti element was preserved for bSi/ TiO_2 -100 °C, bSi/ TiO_2 -200 °C, bSi/ TiO_2 -300 °C, respectively. This finding is consistent with a former study regarding the ability of higher protection layer deposition temperatures to

maintain integrity of the substrate–catalyst interface.^[20] Thus, throughout the rest of this experiment, TiO_2 deposition is performed at 300 °C, unless otherwise noted.

For further confirmation of whether or not one layer of TiO_2 is enough to protect the catalyst from leaching and the substrate from oxidation, we deposited 2 nm of TiO_2 onto the Si/Pt electrode (denoted as Si/Pt/ TiO_2). After 24 h electrolysis, the Si/Pt/ TiO_2 photocathode maintained $\approx 60\%$ retention of its initial photocurrent (Figure 2C). As depicted by SEM in Figure S8 in the Supporting Information, however, Pt aggregation and a slight change in substrate pore size still occur. This result

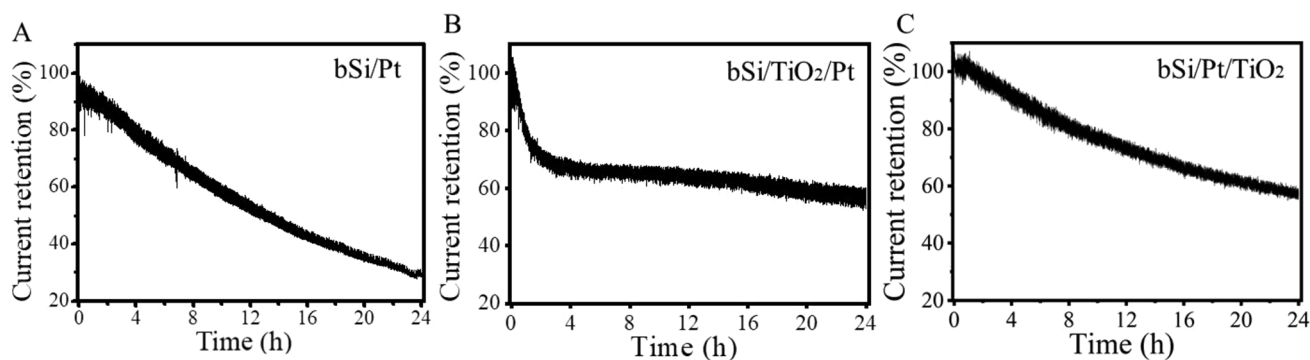
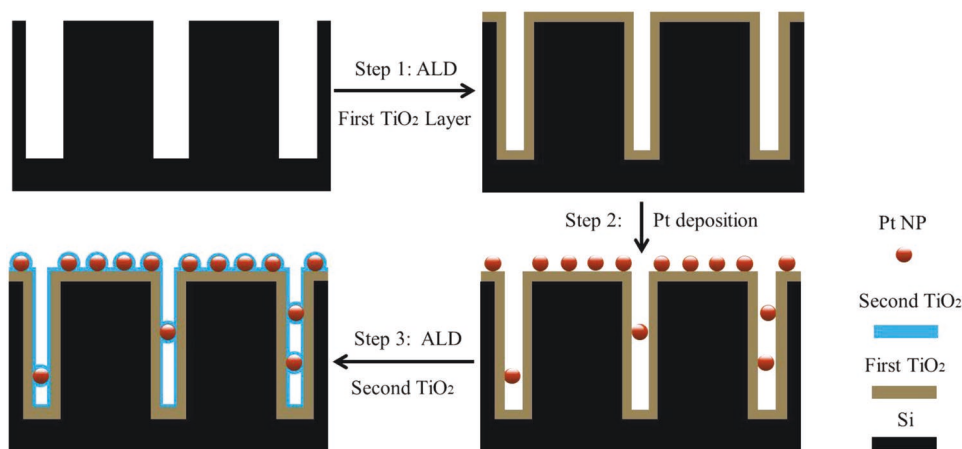


Figure 2. PEC stability testing: photocurrent retention percentage versus time of A) bSi/Pt, B) bSi/ TiO_2 /Pt, and C) bSi/Pt/ TiO_2 electrodes in 0.5 M H_2SO_4 .



Scheme 1. Fabrication diagram of the dual TiO_2 layer protected photocathode. Step 1: ALD deposition of the first TiO_2 layer. Step 2: Electroless deposition of Pt NPs. Step 3: ALD deposition of the second TiO_2 layer.

suggests that 2 nm of TiO_2 on top of the Pt NPs prevents neither the Pt from leaching nor the substrate from oxidizing during prolonged operation. Thus, applying a TiO_2 layer between the substrate and catalyst layers, in addition to the TiO_2 layer on top of the catalyst, is critical to stabilize the photoelectrode–catalyst interface.

The protection strategy proposed herein to fabricate the dual TiO_2 layer electrode, $\text{bSi}/\text{TiO}_2/\text{Pt}/\text{TiO}_2$, is depicted in **Scheme 1**. First, an initial 20 nm TiO_2 layer is deposited onto the nanoporous bSi. Next, the Pt catalyst is deposited on top of the initial TiO_2 layer. Finally, a 2 nm TiO_2 layer is applied on top of $\text{Si}/\text{TiO}_2/\text{Pt}$ interface. Aside from providing protection,

TiO_2 works as an adhesive layer that prevents leaching of Pt catalysts.

Scanning transmission electron microscopy (STEM) imaging (**Figure 3A**) reveals the morphology of the channels in the nanoporous Si. Pt NPs range between ≈ 20 and 100 nm in diameter and randomly decorate the TiO_2 -coated bSi surface (**Figure 3A–C**). Interestingly, some Pt NPs manage to penetrate the nanoporous channels and present themselves at various depths (up to ≈ 300 nm) where contact is made with the nanochannel inner shell (**Figure 3B,C**). Electron dispersive X-ray spectroscopy (EDX) mappings (**Figure S9**, Supporting Information) of bSi nanoporous channels show uniform

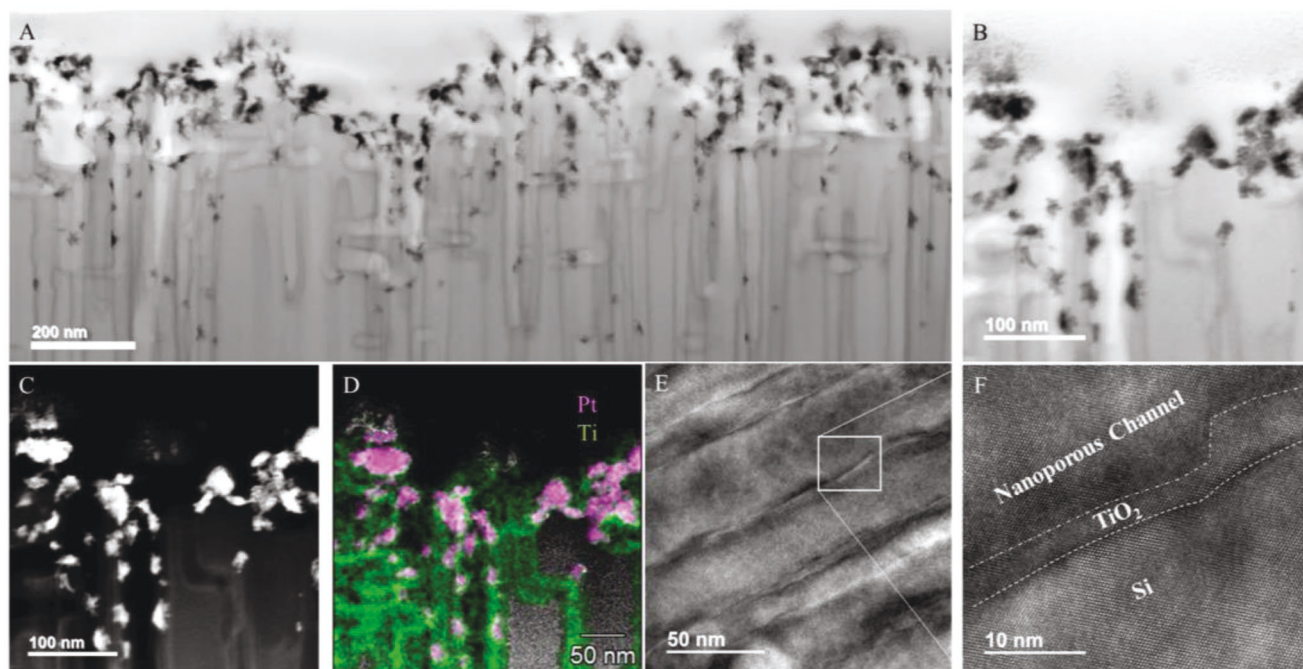


Figure 3. Elemental analysis of the $\text{bSi}/\text{TiO}_2/\text{Pt}/\text{TiO}_2$ photocathode. A–C) High-angle annular STEM images of A) bright field at low magnification, B) bright field at high magnification, and C) dark field at high magnification. D) STEM-based EDX elemental mixed mapping of Pt (pink) and Ti (green). E,F) TEM imaging of $\text{bSi}/\text{TiO}_2/\text{Pt}/\text{TiO}_2$ photocathode at E) low magnification and F) high magnification.

distribution of Ti and O elements. This demonstrates the surface coverage ability of ALD as a gas-phase deposition technique. The overlapped Ti/Pt from EDX mapping shows the Pt NPs (shown in pink, Figure 3D) to coincide with and be wrapped by TiO_2 (shown in green, Figure 3D). This is consistent with the intended procedure to deposit extra TiO_2 on top of the Pt catalysts. Transmission electron microscopy (TEM) was also carried out to study the Si/ TiO_2 interface (Figure 3E,F; Figure S10, Supporting Information) and shows a distinct Si/ TiO_2 interface inside the Si nanochannels. Selective area fast Fourier transforms (FFT) interpret the crystallographic structures that correspond with Si, SiO_2 , and TiO_2 (Figure S10, Supporting Information). Based on Figure S10b,c for the selected area in Figure S10a in the Supporting Information, the structure of TiO_2 was revealed as a coherent portion inside the channel. Based on the lattice spacing, TiO_2 is recognized as having rutile structure with an interatomic spacing of $3.835 \pm 0.080 \text{ \AA}$. This result is distinguished from the anatase (tetragonal) and brookite (orthorhombic) structures of TiO_2 . We have indexed the subunit portion along the direction [110] and [001] for the tetragonal cubic structure shown in Figure S10c in the Supporting Information. From inside the track, Figure S10d in the Supporting Information primarily revealed an arrangement of Si atoms with $5.489 \pm 0.083 \text{ \AA}$. The same spacing corresponding to Si is found in Figure S10e in the Supporting Information as well. A slight change in radial distance occurs at the inner wall in Figure S10f in the Supporting Information, most evident when the TiO_2 and Si

patterns are overlapped. Figure S10g in the Supporting Information shows spots indexed with a small portion of TiO_2 overlapped by Si. The atomic arrangement of the subunits is resolved in Figure S10c in the Supporting Information within the vicinity of the inner wall. The high-resolution imaging and spectroscopic results support the presence of rutile-based TiO_2 neighboring Si. The resulting thickness of TiO_2 is lower than the expected 22 nm due to etching before and after Pt NP deposition causing partial loss of TiO_2 , as previously discussed in this section. Nevertheless, the Si surface, nanochannels, and Pt NPs are well covered with TiO_2 , which is critical to extend the operation lifetime of photoelectrodes.

Our dual TiO_2 protection strategy has proven to be effective in both acidic and basic electrochemical environments. As shown in Figure 4A, the photocurrent retention of the bSi/ TiO_2 /Pt/ TiO_2 photocathode reached 87% in strong acidic solution (0.5 M H_2SO_4). This result is almost three times higher than results achieved by the unprotected Si/Pt (30% initial current maintained), which is almost $\approx 30\%$ better in current retention than the results achieved by the electrodes protected with a single TiO_2 layer (Figure 4B). The unprotected bSi/Pt experienced almost complete loss in activity during the extended 76 h stability test, while the dual layer protected electrode lost only 20% of its activity (Figure S11, Supporting Information). Plus, at least 70% of the initial current is maintained during electrolysis for 110 h (Figure S11, Supporting Information). Shown in Figure 4C, the dual layer protected electrode demonstrates 65% current retention, which is 13 times

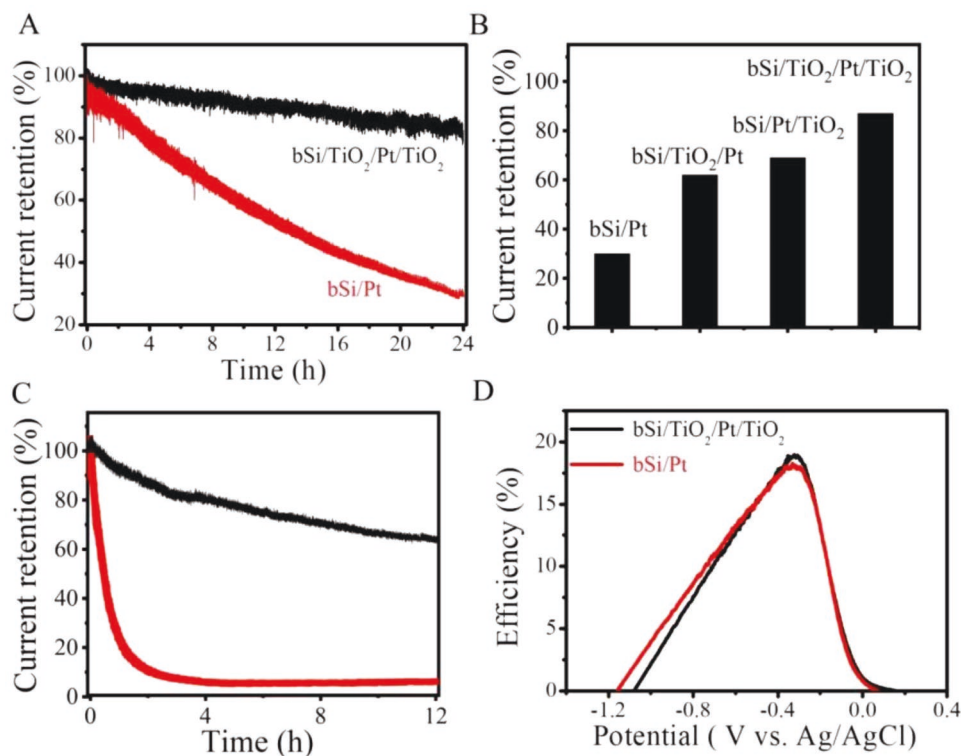


Figure 4. A) PEC stability testing: photocurrent retention percentage versus time of bSi/ TiO_2 /Pt/ TiO_2 and bSi/Pt electrodes in 0.5 M H_2SO_4 for 24 h. B) Photocurrent retention of bSi/Pt, bSi/ TiO_2 /Pt, bSi/Pt/ TiO_2 , and bSi/ TiO_2 /Pt/ TiO_2 electrodes after 24 h electrolysis. C) PEC stability testing: photocurrent retention percentage versus time of bSi/ TiO_2 /Pt/ TiO_2 and bSi/Pt electrodes in 1 M NaOH for 24 h. D) Energy conversion efficiency as a function of applied bias for the bSi/ TiO_2 /Pt/ TiO_2 and bSi/Pt electrodes in 0.5 M H_2SO_4 .

better than the bare bSi/Pt electrode (with only 5% current remaining) after 12 h electrolysis in 1 M NaOH aqueous solution. To better understand if the dual protection strategy influences the charge transfer efficiency, the calculated photon-to-current conversion efficiency of the bSi/Pt and bSi/TiO₂/Pt/TiO₂ photo cathodes is provided in Figure 4D. The dual layer protected electrodes reach a maximum efficiency of ≈18.8% at −0.32 V versus Ag/AgCl and maintain similar efficiencies when compared with the unprotected (bSi/Pt) photocathode (from 0 to −1.2 V). This result suggests that dual TiO₂ layers increase the long-term stability of the bSi/Pt interfaces without sacrificing its efficiency.

Regarding how the top TiO₂ layer's thickness affects stability, in a previous report,^[23] a 15 nm TiO₂ was deposited on top of Si nanowires coated with Pt (bSi/Pt) to protect the interface from corrosion. The results demonstrated stability for only 2 h. Two samples, with 2 and 15 nm of TiO₂ layered on top (samples denoted as bSi/TiO₂/Pt/TiO₂-2 nm and bSi/TiO₂/Pt/TiO₂-15 nm, respectively) were studied in this investigation. Analysis of the results shows the bSi/TiO₂/Pt/TiO₂-15 nm electrode has similar PEC stability to the Si/TiO₂/Pt/TiO₂-2 nm sample (Figure S12, Supporting Information). The linear sweep voltammetry (LSV) performances (Figure S13, Supporting Information) indicate that the 2 nm sample produced a more positive onset potential and saturation potential, compared to the 15 nm sample. Furthermore, electrochemical impedance spectroscopy (EIS) results (Figure S14, Supporting Information) provide a larger semicircle for the 15 nm sample relative to the 2 nm sample. This implies that a 15 nm TiO₂ layer may jeopardize electron transport at the Pt NP/electrolyte interface.^[41] An additional 50 nm intermediate layer was tested as well. The results produce a higher charge transfer resistance, a much worse LSV onset potential, and a larger semicircle when compared with the 20 nm intermediate layer electrode (Figures S15 and S16, Supporting Information).

Next, we investigated whether or not the dual protection layer is able to prevent aggregation and leaching of Pt catalysts, as well as further oxidation of nanoporous Si. For this investigation, the surface morphologies of the bSi/TiO₂/Pt/TiO₂ electrode were studied further, both before and after electrolysis. The density and size of the Pt NPs remained approximately the same after 24 h electrolysis (Figure S17, Supporting Information), which differentiates the dual-layer protected interface from the single-layer protected bSi/TiO₂/Pt, bSi/Pt/TiO₂ (Figures S3 and S8, Supporting Information), and nonprotected bSi/Pt interfaces (Figure 1). After the 110 h test, the Pt NPs maintained their size and approximate density distribution. These results indicate that the additional layer leads to consistent catalytic activity and preservation of interfacial structures.

From our findings, we sought to validate the generality of the proposed strategy. In Figure 5, the dual TiO₂ layer-protected MoS₂ photocathode (bSi/TiO₂/MoS_x/TiO₂) shows a current retention of ≈91%, which was among the most stable MoS₂-based photocathodes that has been reported (Table S2, Supporting Information) to date. This photocurrent retention is much higher than the 20% achieved by the intermediate-layer-protected MoS₂ photocathode (bSi/TiO₂/MoS_x) during its 24 h electrolysis test in 0.5 M H₂SO₄. The greatly improved

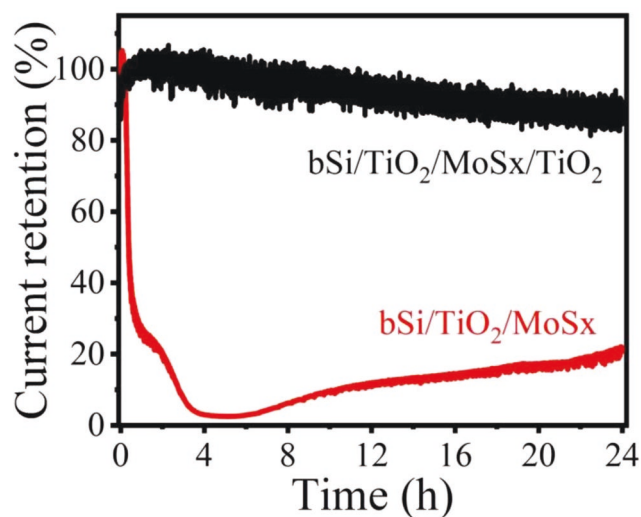


Figure 5. Electrolysis stability testing: photocurrent retention versus time of bSi/TiO₂/MoS_x/TiO₂ and bSi/TiO₂/MoS_x electrodes in 0.5 M H₂SO₄ for 24 h.

stability of the bSi/TiO₂/MoS_x/TiO₂ electrode possibly stems from enhancement of the stability of both the MoS_x catalyst and the Si–MoS_x interface. In summary, we expect this dual layer protection strategy to successfully solve instability issues for a dynamic range of applications and substrate–catalyst interfaces.

3. Conclusions

Previous approaches to photocathode passivation have been limited to the photoabsorber substrate. Here we have demonstrated a dual-layer protection strategy that targets both the substrate and catalyst. The TiO₂ deposition temperature and thickness can dramatically improve the stability and performance of Si/Pt electrodes, as we have reported. In the control experiments under acidic conditions, photocathodes protected with a single layer of TiO₂ show ≈62% and ≈60% photocurrent retentions over 24 h electrolysis. Moreover, the results show an improvement to the 30% photocurrent retention witnessed in the unprotected photocathodes. The dual-layer TiO₂-protected electrodes show improved stability in acidic conditions, maintaining 85% retention of their current produced over 24 h electrolysis and 70% current retention over 110 h electrolysis. These results occur without sacrificing any photon-to-current conversion efficiency. Under alkaline conditions, the dual protected electrodes showed improved stabilization of the Si–Pt interface by maintaining 70% of their performance during electrolysis for 12 h, while the unmodified electrodes lost 95% of their initial current in the first 4 h. In comparison to the 20% current retention achieved by the unprotected MoS_x catalytic system, the dual TiO₂ protection layer demonstrated the ability to sustain 91% of its current retention. These results validate the effectiveness of the proposed protection strategy. Therefore, both intermediate and top protection layers are vital to preserve the longevity of photoelectrode–catalyst interfaces. This TiO₂ dual-layer approach conserves the structure and properties of the semiconductor

and the catalyst and improves their charge transfer properties. The general nature of our proposed protection strategy provides the opportunity to stabilize various heterogeneous catalytic systems for energy conversion applications, enabling PEC systems to be one step closer to economic viability.

4. Experimental Section

Nanoporous bSi Fabrication: 525 μm of boron doped p-type (100) Si wafers with resistivity of 3–5 $\Omega\text{-cm}$ (WaferPro LLC) were used to fabricate nanoporous bSi using the MACE method. Before fabrication, Si wafers were cleaned by sonication in acetone, ethanol, and deionized (DI) water, respectively. The backside of each Si wafer was covered with Kapton tape for protection. In the MACE process, the Si wafers were first immersed in 5 wt% HF for 90 s, to remove any native Si oxides, and then rinsed with DI water. Next, metallic silver NPs were grown on the Si surface via an electroless Ag deposition by soaking the wafer in a 1×10^{-3} M AgNO_3 /1 wt% HF solution for 30 s. This was followed by another DI water rinse. After Ag deposition, the wafers were immediately transferred into a burial solution (50 wt% HF, 30 wt% H_2O_2 , and DI water with a volumetric ratio of 25:6:370) for 6 min, and then cleaned with DI water. This forms the nanoporous structure. Afterwards, the wafers were placed in 35 wt% HNO_3 solution for 6 min, to remove the Ag particles from the pores. Finally, the wafers were put back into 5 wt% HF for 30 s to remove the oxides formed during the fabrication process, followed by DI water rinse and subsequent dipping into a 0.5 wt% tetramethylammonium hydroxide (TMAH) solution for 2 s to remove the very top sharp layer of the produced nanoporous bSi.

PEC Electrode Fabrication: In this work, four types of PEC electrodes were fabricated. Processed and nonprocessed Si wafers were cut into appropriately sized pieces (0.1–0.3 cm^2). The backside of the sample was first rinsed with water and etched in 5 wt% HF for 30 s to remove surface oxides. Next, a commercial Ga–In eutectic alloy thin layer was applied onto the backside of the sample to make an ohmic contact. The backside of the sample was then pressed to a Cu wire spiral-coated with conductive silver paint. Afterwards, to provide the assembly with a mechanically stable body, the Cu wire tail was passed through a glass tube, with the spiral wire and Si sample head assembly left outside of the tube. Finally, the resulting electrode assembly was electrically insulated by covering any exposed copper/silver paint and the electrode head-glass tube junction with Loctite 9462 epoxy. After drying overnight, a second layer of Loctite 120 epoxy was applied for experiments involving long-term electrolysis. The produced photoelectrodes have exposed volumetric areas of 0.1–0.3 cm^2 . For Pt NP deposition, the fabricated electrode was first etched in 5 wt% HF for 30 s and washed with DI water, and then soaked in 5×10^{-3} M K_2PtCl_6 /1 wt% HF solution for 60 s. The Pt NPs distribution was analyzed using Image J software (<https://imagej.nih.gov/ij/>). Amorphous MoS_x thin films were prepared by electrodeposition at -0.3 V versus Ag/AgCl in an aqueous electrolyte containing 5×10^{-3} M of $[(\text{NH}_4)_2\text{MoS}_4]$ and 0.5 M Na_2SO_4 under one sun illumination for 20 min. After the deposition, the electrode was cleaned with distilled water.

Atomic Layer Deposition of TiO_2 : All ALDs of TiO_2 were carried out with the GEMStar XT Atomic Layer Deposition System. The internal gas lines of the system were heated at 110 $^\circ\text{C}$ to avoid condensation. The chambers were set with deposition temperatures of 100, 200, and 300 $^\circ\text{C}$, respectively. Titanium (IV) isopropoxide (TTIP) and H_2O were used as the titanium and oxygen precursors. The deposition process was performed with the following sequence: 0.1 s TTIP pulse, 15 s exposure, 30 s N_2 purge, 0.05 s H_2O pulse, 15 s exposure, 30 s N_2 purge.

STEM Sample Preparation: Electron transparent TEM thin foils were prepared using an FEI Helios Dual Beam focus ion beam (FIB) instrument. Samples were coated with a layer of carbon to improve sample conductivity and to minimize sample drift inside the FIB. Within the FIB, grained ion beam platinum layers (with the gradient ranging

from fine to coarse) were deposited over of an area 15 by 3 μm , with a thickness of 3 μm . After lift out, the final lamellae was measured as 13 by 5 μm . Less than 100 nm in total thickness was lifted and mounted to a molybdenum Omni probe TEM grid for examination. A final cleaning step was performed using a 5 kV gallium beam, with a beam current of 12 pA, to remove material deposits during FIB preparation and reduce milling damage.

Electron Microscopy Characterizations: The prepared and modified nanoporous Si sample morphologies were characterized using an FEI Quanta 450 FEG microscope at 20 kV with a spot size of 3.0. A JEOL 2800 TEM, equipped with dual high solid angle 30 mm^2 windowless Si X-ray detectors, was operated in high resolution TEM and STEM modes at 200 kV. For STEM analysis, a nanometer-sized probe, with a total beam current of less than 110 pA, was employed for sample analysis using the inelastically scattered electrons passing through the electron transparent sample to form a high angle annular dark field (HAADF) image, which was proportional to atomic mass. EDX was operated under the same conditions to acquire the Si-K, Ti-K/L, O-K, and Pt-L characterizations with the best achievable spatial and energy resolution. To acquire quantitative measures in a single acquisition, Multiple 10 s scans over 256×256 pixels were performed to acquire measurements in a single acquisition. Cliff–Lorimer thin film correction and Thermo Scientific software were used to process the EDX spectra and calculate weighted atomic percent spectral maps. Weighted spectral images were visualized using Matlab. These nominalized maps were compared against the accompanying HAADF image, allowing the quantitative differences of particles, tracks, and pores to be visualized.

Photoelectrochemical Measurements: All PEC measurements were performed with a CHI 660E Electrochemical Workstation using a steady DC-powered 150 W Xe-arc lamp (New Port) light source. A water filter was used to block the infrared irradiation and the incident light intensity was calibrated to 100 mW cm^{-2} (equivalent to one sun) using a Si photodiode. For all experiments, Ag/AgCl (3 M NaCl, BASI) and a Pt coil were used as reference and counter electrodes, respectively. All tests were carried out in a homemade electrochemical cell in which working, reference, and counter electrodes were in different compartments connected using a salt bridge isolated by a glass frit between each electrolysis compartment. LSV measurements were performed across the range from 0.2 to -2 V versus Ag/AgCl (0.5 M H_2SO_4) and from -0.4 to -2 V versus Ag/AgCl (1 M NaOH), with a scanning rate of 100 mV s^{-1} . PEC electrolysis stability tests were performed within -0.4 to -0.5 V versus Ag/AgCl (0.5 M H_2SO_4) and -1.4 to -1.5 V versus Ag/AgCl (1 M NaOH), based on each photocathode's saturation potential. EIS measurements were carried out at -0.1 V versus Ag/AgCl, with 5 mV variation in the frequency range of 1– 10^6 Hz and 12 steps per decade. All fabricated electrodes were first etched with 5 wt% HF for 30 s and cleaned with DI H_2O before testing.

Onset potential was extracted from the LSV tests, which was equal to the potential where the photocurrent started increasing, i.e., 0.05 mA cm^{-2} . Saturation potential was defined as the potential where photocurrent was saturated and no longer increasing.

The photon-to-current conversion efficiency (η) of the produced photocathode was calculated based on the following equation:

$$\eta = \frac{J_p (1.23 - |V_{\text{working}} - V_{\text{oc}}|)}{P_{\text{in}}}$$

where J_p is the photocurrent density, V_{working} is the applied voltage on the working electrode, V_{oc} is the open circuit potential of working electrode, and P_{in} is the incident light power (100 mW cm^{-2} in this work).

Supporting Information

Supporting Information is available from the Wiley Online Library or from the author.

Acknowledgements

The authors acknowledge SDSU startup funds, the SDSU University Grants Program, and NSF award CBET-1704992 for their support in this research. Y.Z. acknowledges the financial support through the National Natural Science Foundation of China within project No. 21771004. L.Z. thanks the financial support from the National Natural Science Foundation of China (No. 21575099). J.A.A. was partially supported by the INL Laboratory Directed Research & Development (LDRD) Program under DOE Idaho Operations Office Contract DE-AC07-05ID14517.

Conflict of Interest

The authors declare no conflict of interest.

Keywords

atomic layer deposition, nanoporous silicon, photoelectrochemistry, TiO₂

Received: December 27, 2018

Revised: January 25, 2019

Published online: February 26, 2019

- [1] J. Barber, *Chem. Soc. Rev.* **2009**, 38, 185.
- [2] International Energy Agency, *World Energy Outlook 2017*, OECD Publishing, Paris/IEA, Paris **2017**.
- [3] S. Hu, N. S. Lewis, J. W. Ager, J. Yang, J. R. McKone, N. C. Strandwitz, *J. Phys. Chem. C* **2015**, 119, 24201.
- [4] C. Jiang, S. J. A. Moniz, A. Wang, T. Zhang, J. Tang, *Chem. Soc. Rev.* **2017**, 46, 4645.
- [5] B. Parida, S. Iniyar, R. Goic, *Renewable Sustainable Energy Rev.* **2011**, 15, 1625.
- [6] M. G. Walter, E. L. Warren, J. R. McKone, S. W. Boettcher, Q. Mi, E. A. Santori, N. S. Lewis, *Chem. Rev.* **2010**, 110, 6446.
- [7] J. Bian, Q. Li, C. Huang, J. Li, Y. Guo, M. Zaw, R. Q. Zhang, *Nano Energy* **2015**, 15, 353.
- [8] J. Bian, L. Xi, J. Li, Z. Xiong, C. Huang, K. M. Lange, J. Tang, M. Shalom, R. Q. Zhang, *Chem. - Asian J.* **2017**, 12, 1005.
- [9] J. Bian, L. Xi, C. Huang, K. M. Lange, R. Q. Zhang, M. Shalom, *Adv. Energy Mater.* **2016**, 6, 1600263.
- [10] R. L. House, N. Y. M. Iha, R. L. Coppo, L. Alibabaei, B. D. Sherman, P. Kang, M. K. Brennaman, P. G. Hoertz, T. J. Meyer, *J. Photochem. Photobiol., C* **2015**, 25, 32.
- [11] K. Q. Peng, X. Wang, L. Li, Y. Hu, S. T. Lee, *Nano Today* **2013**, 8, 75.
- [12] U. Sim, H. Y. Jeong, T. Y. Yang, K. T. Nam, *J. Mater. Chem. A* **2013**, 1, 5414.
- [13] S. Chen, L. W. Wang, *Chem. Mater.* **2012**, 24, 3659.
- [14] D. Zhang, J. Shi, W. Zi, P. Wang, S. F. Liu, *ChemSusChem* **2017**, 10, 4324.
- [15] K. Sun, S. Shen, Y. Liang, P. E. Burrows, S. S. Mao, D. Wang, *Chem. Rev.* **2014**, 114, 8662.
- [16] J. Oh, T. G. Deutsch, H. C. Yuan, H. M. Branz, *Energy Environ. Sci.* **2011**, 4, 1690.
- [17] Y. Zhao, N. C. Anderson, K. Zhu, J. A. Aguiar, J. A. Seabold, J. van de Lagemaat, H. M. Branz, N. R. Neale, J. Oh, *Nano Lett.* **2015**, 15, 2517.
- [18] L. Santinacci, M. W. Diouf, M. K. S. Barr, B. Fabre, L. Joanny, F. Gouttefangeas, G. Loget, *ACS Appl. Mater. Interfaces* **2016**, 8, 24810.
- [19] Y. Yu, Z. Zhang, X. Yin, A. Kvit, Q. Liao, Z. Kang, X. Yan, Y. Zhang, X. Wang, *Nat. Energy* **2017**, 2, 17045.
- [20] B. Seger, T. Pedersen, A. B. Laursen, P. C. K. Vesborg, O. Hansen, I. Chorkendorff, *J. Am. Chem. Soc.* **2013**, 135, 1057.
- [21] S. Hu, M. R. Shaner, J. A. Beardslee, M. Lichterman, S. Bruce, N. S. Lewis, *Science* **2014**, 344, 1005.
- [22] M. J. Choi, J. Y. Jung, M. J. Park, J. W. Song, J. H. Lee, J. H. Bang, *J. Mater. Chem. A* **2014**, 2, 2928.
- [23] S. Li, P. Zhang, X. Song, L. Gao, *ACS Appl. Mater. Interfaces* **2015**, 7, 18560.
- [24] N. Guijarro, M. S. Prévot, K. Sivula, *Phys. Chem. Chem. Phys.* **2015**, 17, 15655.
- [25] Z. Yin, R. Fan, G. Huang, M. Shen, *Chem. Commun.* **2017**, 54, 543.
- [26] R. Fan, W. Dong, L. Fang, F. Zheng, M. Shen, *J. Mater. Chem. A* **2017**, 5, 18744.
- [27] F. Yang, M. Abadia, C. Chen, W. Wang, L. Li, L. Zhang, C. Rogero, A. Chuvilin, M. Knez, *Nano Res.* **2017**, 10, 97.
- [28] X. Q. Bao, D. Y. Petrovykh, P. Alpuim, D. G. Stroppa, N. Guldris, H. Fonseca, M. Costa, J. Gaspar, C. Jin, L. Liu, *Nano Energy* **2015**, 16, 130.
- [29] C. J. Chen, K. C. Yang, C. W. Liu, Y. R. Lu, C. L. Dong, D. H. Wei, S. F. Hu, R. S. Liu, *Nano Energy* **2017**, 32, 422.
- [30] L. Zhang, C. Liu, A. B. Wong, J. Resasco, P. Yang, *Nano Res.* **2015**, 8, 281.
- [31] F. Nandjou, S. Haussener, *J. Phys. D: Appl. Phys.* **2017**, 50, 124002.
- [32] D. Bae, B. Seger, P. C. K. Vesborg, O. Hansen, I. Chorkendorff, *Chem. Soc. Rev.* **2017**, 46, 1933.
- [33] M. Li, Y. Li, W. Liu, L. Yue, R. Li, Y. Luo, M. Trevor, B. Jiang, F. Bai, P. Fu, Y. Zhao, C. Shen, J. M. Mbengue, *Mater. Res. Bull.* **2016**, 76, 436.
- [34] X. Liu, P. R. Coxon, M. Peters, B. Hoex, J. M. Cole, D. J. Fray, *Energy Environ. Sci.* **2014**, 7, 3223.
- [35] H. Han, Z. Huang, W. Lee, *Nano Today* **2014**, 9, 271.
- [36] Z. Huang, N. Geyer, P. Werner, J. De Boor, U. Gösele, *Adv. Mater.* **2011**, 23, 285.
- [37] T. W. Hansen, A. T. Delariva, S. R. Challa, A. K. Datye, *Acc. Chem. Res.* **2013**, 46, 1720.
- [38] Y. A. Buslaev, V. A. Bochkareva, N. S. Nikolaev, *Bull. Acad. Sci. USSR, Div. Chem. Sci. (Engl. Transl.)* **1962**, 11, 361.
- [39] C. Guerra-Núñez, Y. Zhang, M. Li, V. Chawla, R. Erni, J. Michler, H. G. Park, I. Utke, *Nanoscale* **2015**, 7, 10622.
- [40] M. Reiners, K. Xu, N. Aslam, A. Devi, R. Waser, S. Hoffmann-Eifert, *Chem. Mater.* **2013**, 25, 2934.
- [41] Z. Huang, C. Wang, L. Pan, F. Tian, X. Zhang, C. Zhang, *Nano Energy* **2013**, 2, 1337.